

**Figure 5** The change of ECL spectrum with time after application of 30 V to the cell. A solution of 25 mM DPA in DMF was introduced with a flow rate of  $20 \mu\text{L min}^{-1}$ . The spectra were sequentially measured with a 50-ms exposure time from just before the application of 30 V. The actual cavity length was  $1.9 \mu\text{m}$ . Inset, the time decay of the peak height located at  $\sim 435 \text{ nm}$ . The time origin is the last time at which the ECL signal was within the noise level. The labels correspond to those on the ECL spectra.

bright in the initial stage and then its intensity gradually decreases. This is because the concentration of the ground-state DPA is very high near the electrode and generates a higher concentration of excited-state DPA than that in the steady state. The temporal change in peak intensity at 435 nm is shown in the inset. The decay time was 0.071 s. This long decay, resulting from the continuous supply of dye molecules, depended on the flow rate and applied voltage.

In the low-intensity spectrum (trace c in Fig. 5), the peaks at 405 and 435 nm are almost the same height. However, in the high-intensity spectrum (trace b in Fig. 5), the peak at 435 nm is greatly amplified compared with the peak at 405 nm. The linewidth (full-width at half-maximum) of the peak at 435 nm decreased  $\sim 25\%$ . The peak at 405 nm merged with the peak at 435 nm when the intensity increased further (trace a in Fig. 5). The merged peak still shows line narrowing with increasing ECL intensity. For example, the FWHM of the peak at the highest intensity (at 200-ms in the inset) is  $\sim 32\%$  narrower than that at lower intensity (300 ms). These spectrum changes as a function of intensity clearly indicate a stimulated emission.

The results shown in Figs 3–5 indicate that the lasing was achieved by an electrochemical reaction. This is supported by another experiment in which fringe patterns were observed when the half-mirror was replaced with an interdigitated array electrode which functioned as a grating. Much clearer lasing could be observed by either decreasing the distance between the electrodes of the flow cell to the order of a wavelength, or increasing their reflectivity. □

Received 9 June 1997; accepted 9 June 1998.

1. Feldberg, S. W. Theory of controlled potential electrogeneration of chemiluminescence. *J. Am. Chem. Soc.* **88**, 390–393 (1966).
2. Maloy, J. T., Prater, K. B. & Bard, A. J. Electrogenerated chemiluminescence. II. The rotating ring-disk electrode and the pyrene-N,N,N',N'-tetramethyl-p-phenylenediamine system. *J. Phys. Chem.* **72**, 4348–4350 (1968).
3. Keszthelyi, C. P., Tokel-Takvoryan, N. E. & Bard, A. J. Electrogenerated chemiluminescence: Determination of the absolute luminescence efficiency in electrogenerated chemiluminescence. 9,10-Diphenylanthracene-thianthrene and other systems. *Anal. Chem.* **47**, 249–256 (1975).
4. Bartelt, J. E., Drew, S. M. & Wightman, R. M. Electrochemiluminescence at band array electrodes. *J. Electrochem. Soc.* **139**, 70–74 (1992).
5. Collinson, M. M., Pastore, P., Maness, K. M. & Wightman, R. M. Electrochemiluminescence interferometry at microelectrodes. *J. Am. Chem. Soc.* **116**, 4095–4096 (1994).
6. Schaper, H., Koestlin, H. & Schneider, E. New aspects of d.c. electrochemiluminescence. *J. Electrochem. Soc.* **129**, 1289–1294 (1982).
7. Measures, R. M. Prospects for developing a laser based on electrochemiluminescence. *Appl. Opt.* **13**, 1121–1133 (1974).
8. Measures, R. M. Physical constraints associated with the development of a laser based on electrochemiluminescence. *Appl. Opt.* **14**, 909–916 (1975).

9. Heller, C. A. & Jernigan, J. L. Electrochemical pumping of laser dyes. *Appl. Opt.* **16**, 61–66 (1977).
10. Myer, J. A., Johnson, C. L., Kierstead, E., Sharma, R. D. & Itzkan, I. Dye laser stimulation with a pulsed  $\text{N}_2$  laser line at 3371 Å. *Appl. Phys. Lett.* **16**, 3–5 (1970).
11. Ujihara, K. A simple relationship between directivity and linewidth of a planar microcavity laser. *Jpn. J. Appl. Phys.* **33**, 1059–1060 (1994).
12. Hakki, B. W. & Paoli, T. L. CW degradation at 300 K of GaAs double-heterostructure junction lasers. II. Electronic gain. *J. Appl. Phys.* **44**, 4113–4119 (1973).
13. Hakki, B. W. & Paoli, T. L. Gain spectra in GaAs double-heterostructure injection lasers. *J. Appl. Phys.* **46**, 1299–1306 (1975).

**Acknowledgements.** We are grateful to M. Morita for encouragement and support.

Correspondence and requests for materials should be addressed to T.H. (e-mail: horiuchi@will.brl.nitt.co.jp).

## Effects of orbital decay on satellite-derived lower-tropospheric temperature trends

Frank J. Wentz & Matthias Schabel

Remote Sensing Systems, 438 First Street, Suite 200, Santa Rosa, California 95401, USA

The 17-year lower-tropospheric temperature record derived from the satellite Microwave Sounding Unit (MSU)<sup>1–3</sup> shows a global cooling trend, from 1979 to 1995, of  $-0.05 \text{ K per decade}$  at an altitude of about 3.5 km (refs 4, 5). Air temperatures measured at the Earth's surface, in contrast, have risen by approximately  $+0.13 \text{ K per decade}$  over the same period<sup>4,6</sup>. The two temperature records are derived from measurements of different physical parameters, and thus are not directly comparable. In fact, the lower stratosphere is cooling substantially (by about  $-0.5 \text{ K per decade}$ )<sup>5</sup>, so the warming trend seen at the surface is expected to diminish with altitude and change into a cooling trend at some point in the troposphere. Even so, it has been suggested that the cooling trend seen in the satellite data is excessive<sup>4,7,8</sup>. The difficulty in reconciling the information from these different sources has sparked a debate in the climate community about possible instrumental problems and the existence of global warming<sup>4,7,9</sup>. Here we identify an artificial cooling trend in the satellite-derived temperature series caused by previously neglected orbital-decay effects. We find a new, corrected estimate of  $+0.07 \text{ K per decade}$  for the MSU-based temperature trend, which is in closer agreement with surface temperatures. We also find that the reported<sup>7</sup> cooling of the lower troposphere, relative to the middle troposphere, is another artefact caused by uncorrected orbital-decay effects.

The debate within the climate community<sup>4,7,9</sup> about differences between the global temperature trends determined from *in situ* surface records and from lower-tropospheric MSU satellite data has centred on two fundamental issues: physical differences between the two measurements and possible instrumental artefacts. MSU middle tropospheric temperature measurements (MSU2) represent a vertically weighted air temperature centred at an altitude of  $\sim 7 \text{ km}$ , while the MSU lower-tropospheric temperature (MSU2R) weighting function peaks around 3.5 km. MSU2, MSU2R and *in situ* surface temperatures are therefore not directly comparable, and their decadal trends are thus not expected to be identical, particularly as the lower stratosphere is known to be cooling substantially<sup>5</sup>. However, the large difference between global surface and MSU2R temperature trends ( $+0.13 \text{ K per decade}$  and  $-0.05 \text{ K per decade}$ , respectively<sup>4–6</sup>) is difficult to explain. In the tropics the difference is even more pronounced, with sea surface temperatures rising by  $+0.10 \text{ K per decade}$  and MSU2R falling by  $-0.11 \text{ K per decade}$ <sup>7</sup>. The

magnitude of these differences has led to the suggestion<sup>4,7,8</sup> that the reported MSU2R cooling trend, particularly in the tropics, is excessive.

In addition to the concern over excessive cooling of MSU2R compared to *in situ* data, there is another more obvious problem: MSU2R, centred at around 3.5 km altitude, is cooling at  $-0.17$  K per decade relative to MSU2, centred at around 7 km (ref. 7). This strong relative cooling disagrees with radiosonde data that show little relative difference in the temperature trends observed at 850, 700 and 500 mbar levels<sup>10</sup> (corresponding to altitudes of 1.4, 3.0 and 5.6 km). Recent radiosonde results derived for the MSU time period confirm this observation: the temperature trends of  $-0.01$ ,  $-0.07$  and  $-0.05$  K per decade for 850, 700 and 500 mbar levels, respectively (D. Parker, personal communication) are fairly similar. These values indicate that the lower troposphere (850–700 mbar) is slightly warming relative to the middle troposphere (700–500 mbar), which disagrees with the very large cooling of MSU2R relative to MSU2. The discrepancy between the relative trends in the satellite and radiosonde data is particularly difficult to explain, considering that 20% of the MSU2R signal comes from the surface (discussed below), which is warming, while a substantial fraction of the MSU2 signal comes from the lower stratosphere, which is cooling. This seemingly unphysical cooling of MSU2R relative to MSU2 led us to examine closely the derivation of the two parameters, thereby uncovering a subtle effect related to orbital decay that significantly affects MSU2R but not MSU2.

MSU tropospheric temperatures are derived from measurements of Earth's radiance at 53.74 GHz (MSU channel 2). The MSU sensor scans perpendicular to the satellite subtrack, with 11 footprints extending over a range of incidence angles from  $0^\circ$  to  $55^\circ$ . The MSU2 middle-tropospheric temperature is found from a limb-corrected average of the central 9 footprints. MSU2 has a broad

vertical weighting function centred at  $\sim 7$  km but retaining appreciable weight from the surface well into the stratosphere. To retrieve an air temperature that is more indicative of the lower troposphere, a deconvolution is performed, making use of the fact that the weighting function for the near-limb observations ( $44^\circ$  to  $55^\circ$ ) peaks somewhat higher in altitude than for the near-nadir observations ( $22^\circ$  to  $33^\circ$ ). The MSU2R lower-troposphere temperature  $T_{2R}$  is calculated from the following equation<sup>2</sup>:

$$T_{2R} = 4T_N - 3T_L \quad (1)$$

where  $T_N$  and  $T_L$  are the near-nadir and near-limb observations, respectively. In principle, this linear combination of  $T_N$  and  $T_L$  leads to an effective weighting function centred near 3.5 km.

Our investigation reveals that the unphysical cooling of MSU2R relative to MSU2 is a direct result of  $T_L$  warming relative to  $T_N$ . In the tropics from 1979 to 1995,  $T_N$  and  $T_L$  increased by  $+0.05$  K per decade and  $+0.10$  K per decade, respectively, resulting in an MSU2R trend of  $-0.11$  K per decade. Thus, although  $T_N$  and  $T_L$  are both warming, MSU2R exhibits a cooling trend arising from the extrapolation to the lower troposphere. The question then becomes: why is  $T_L$  warming by  $+0.05$  K per decade relative to  $T_N$ ?

All of the NOAA polar orbiting platforms carrying the MSU instruments lose altitude after launch. In constructing the MSU time series, the satellites are sequentially intercalibrated, so the effect of altitude decrease of one satellite is added onto the next. Figure 1 shows the altitude changes of NOAA-6 to NOAA-14 referenced to a common baseline (NOAA-8 is excluded because it was not used in the MSU time series). Absolute orbital altitudes found from two-line orbital element data provided by NORAD are plotted in Fig. 1 inset. Immediately apparent in the figure is the presence of two intervals, 1979–83 and 1989–92, with dramatically steeper slopes. These intervals correspond to periods during which solar activity was at a maximum<sup>11</sup>. Higher levels of solar ultraviolet radiation during these periods heat the upper atmosphere and increase the drag on the spacecraft. Over intervals of high solar activity, the observed orbital decay rate is  $\sim 2$  km  $\text{yr}^{-1}$ , while periods of low solar activity show a smaller rate of  $0.3$  km  $\text{yr}^{-1}$ . Over the entire 17-year record there is a net drop of 20 km, equivalent to an average rate of  $1.2$  km  $\text{yr}^{-1}$ .

This decrease in altitude is significant because it leads to a corresponding decrease in the Earth incidence angle due to the sphericity of the Earth's surface. For the near-nadir observations, the incidence angle decreases by  $0.0049^\circ \text{yr}^{-1}$  on average, while the near-limb angle changes by more than twice as much ( $0.0120^\circ \text{yr}^{-1}$ ). Radiative transfer calculations<sup>12</sup> show that these changes in incidence angle increase  $T_N$  and  $T_L$  by  $+0.008$  K per decade and  $+0.052$  K per decade, respectively. Thus the orbital decay causes  $T_L$  to warm relative to  $T_N$  at a rate of  $0.044$  K per decade, in close agreement with the anomalous trend mentioned above. Calculations were performed for several atmospheric profiles (high latitudes, mid-latitudes and tropics) and for both land and ocean surfaces. The land emissivity was fixed at 0.85, and the ocean emissivity comes from a microwave ocean model<sup>12</sup>. Atmospheric absorption due to oxygen and water vapour is based on a standard microwave propagation model<sup>13</sup>. The orbital decay correction is insensitive ( $\pm 0.007$  K per decade) to latitude, surface type, and the details of the radiative transfer model. Considering the error in specifying the altitude decay and the small variability due to surface type and latitude, the error in specifying the orbital decay correction is  $\pm 0.01$  K per decade at a 95% confidence level.

Removing the effect of orbital decay, we find that the corrected  $T_N$  and  $T_L$  are both warming at nearly the same rate. In view of their very broad weighting functions, with centroids differing by only 1 km, it seems quite reasonable that the two should have similar trends. Substituting the corrected values of  $T_N$  and  $T_L$  in equation (1) results in a  $+0.12$  K per decade global correction to MSU2R for the 1979–95 period. Adding this correction to the previously

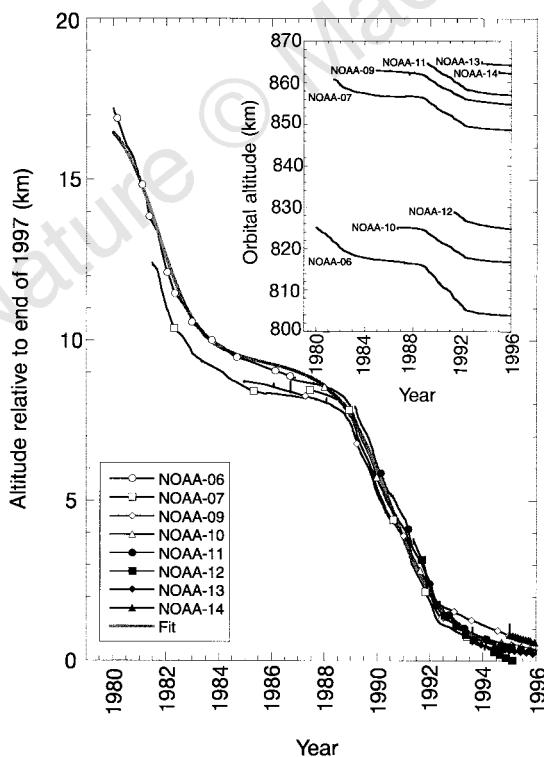


**Figure 1** Cumulative orbital decays for NOAA satellites from 1979 to 1996. Data for all satellites used in the MSU lower-tropospheric temperature series are plotted, shifted by constant offsets to correct for differences in orbital altitude. An empirical nonlinear regression to the data is shown by the grey curve. Absolute altitudes are shown in the inset. (Data shown in this figure are available at <http://www.grove.net/~tkelso/NORAD/archives>)

reported trends ( $-0.11$  K per decade in the tropics and  $-0.05$  K per decade globally) results in new trends of  $+0.01$  K per decade in the tropics and  $+0.07$  K per decade globally.

The decay correction varies from year to year, being greatest during periods of maximum solar activity. Figure 2 shows the effect of orbit decay on trends in MSU2R tropical average ( $20^{\circ}\text{S}$ – $20^{\circ}\text{N}$ ) anomaly time series<sup>7</sup>. Horizontal bars at the top of the figure indicate the periods of high solar activity. To calculate the decay correction, plotted in Fig. 2c, the altitude data for NOAA-6 and NOAA-10, which taken together span the entire 17-year period, were merged at the beginning of 1987. The resulting curve was regressed to an empirical function (the broad grey line in Fig. 1) and used to compute the geometrical correction to MSU2R. Figure 2a shows the time series for the uncorrected MSU2R temperature anomalies (dashed), with its downward trend of  $-0.11$  K per decade. The corrected MSU2R time series is plotted as the solid line. Figure 2b shows the difference between MSU2R and MSU2 temperature anomalies, with and without the correction for orbital decay (solid and dashed lines, respectively). MSU2 is much less sensitive to the effect of orbit decay, serving as a reference for evaluating this effect on MSU2R. Clearly evident in this figure is the cooling of the uncorrected MSU2R relative to MSU2 that occurs during the two periods of high solar activity, and correspondingly large orbital decay. The correlation coefficient between the uncorrected MSU2R–MSU2 difference and the decrease in satellite altitude is 0.91. To compute this correlation, the MSU2R–MSU difference is first smoothed with a gaussian smoothing function with a 180-day standard deviation. The high correlation is strong evidence that the cooling of MSU2R during 1979–83 and 1989–92 is due to orbital decay.

Although orbital decay affects other satellite instruments, it is the unavoidable noise amplification associated with the MSU2R deconvolution procedure and the very small decadal trends being sought which makes this particular data set so sensitive. Other satellite-measured parameters will probably be much less affected. For example, the net spurious warming introduced into MSU2 is only  $+0.008$  K per decade. Nevertheless, the effect is easily computed and should be accounted for in future analyses of satellite data.

Despite the much improved consistency between MSU2 and MSU2R and the closer agreement of the MSU2R record with surface temperature data, there remain some questions which are not entirely resolved by our correction. The main issue is the reported<sup>9</sup> good agreement between the MSU2R (before correction) and radiosonde measurements. Both data sets implied a lower-tropospheric temperature trend of about  $-0.05$  K per decade. However,

these comparisons did not account for surface effects. MSU2R is not simply a measure of the lower-troposphere temperature, but also contains an Earth surface emission component. This sensitivity of MSU2R to surface emissions results from the factor of 4 applied to  $T_N$  in equation (1). We use the radiative transfer model to simulate this sensitivity. The model assumes the Earth's surface temperature changes by 1 K while the temperature at an altitude of 1.5 km (850 mbar) remains constant. Between the surface and 850 mbar, the change linearly decreases to 0 K. The increase of 1 K in the near-surface temperature produces increases of 0.25 K and 0.17 K in the MSU2R-derived temperature ( $T_{2R}$ ) for land and ocean surfaces, respectively, even though the lower-tropospheric temperature remains constant. Thus, on average,  $\sim 20\%$  of the observed trends of  $T_{2R}$  will be due to near-surface trends, and the remainder will be due to trends in the lower and middle troposphere (850–300 mbar). The MSU2 product, which approximately equals  $T_N$ , is much less sensitive to surface effects because of the absence of the factor of 4 in equation (1). Therefore, to directly compare MSU2R with radiosondes, a surface temperature layer is added to the radiosonde layers, and a vertical integration over all layers is done to compute an effective MSU2R trend of  $-0.02$  K per decade (D. Parker, personal communication), which is in closer agreement with the observed  $+0.07$  K per decade trend.

In interpreting these results it is important to consider the uncertainties in estimating decadal trends from MSU and radiosondes. The error in the MSU2R trend is estimated to be  $\pm 0.05$  K per decade at a confidence level of 80% (J. Christy, personal communication). This error was determined by comparing the results of using different combinations of satellites and by reconstructing the time series with random variations of inter-satellite biases. There is a good deal of subjectivity in the MSU error analysis, and, as we show here, there is the possibility that the true error bar is larger due to other, yet to be discovered, effects. The MSU error estimate does not include the  $\pm 0.01$  K per decade uncertainty in specifying the orbit decay correction. This uncertainty must be added to the overall error bar. The error in the radiosonde trend is  $\pm 0.10$  K per decade at a 95% confidence level (D. Parker, personal communication). In this case, the error bars are based on standard least-squares theory but take account of the autocorrelation of the residuals from the linear trend. The error estimates do not allow for systematic biases in the data or for the geographical sparsity of sampling<sup>14</sup>. So again, there is the possibility that the true error is larger. Thus, considering the size and uncertainty of the error bars, the disagreement of 0.09 K per decade between MSU2R and radiosondes may not be too significant.

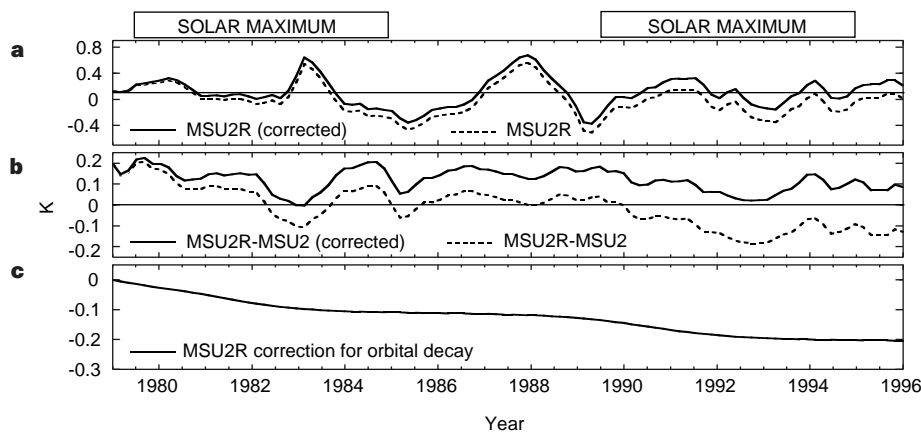


**Figure 2** Effect of correction for orbital decay on MSU2R lower-tropospheric temperature anomalies. **a**, Time series for tropical average ( $20^{\circ}\text{S}$ – $20^{\circ}\text{N}$ ) MSU2R lower-tropospheric temperature anomalies with (solid line) and without (dashed line) the correction for orbital decay. **b**, Differences between the lower-(MSU2R)

and mid-(MSU2) tropospheric temperatures, plotted as in **a**, **c**. The orbital correction to MSU2R based on the data in Fig. 1 (data in this figure adapted from Fig. 1 of ref. 7).

The orbit decay correction of +0.12 K per decade is a relatively simple, though easily overlooked, geometric effect resulting from decreasing satellite altitude. This correction eliminates the spurious cooling of MSU2R during 1979–83 and 1989–92 as well as the spurious cooling of the lower troposphere relative to the middle troposphere. The correction also leads to an overall global warming trend of +0.07 K per decade for the 1979–95 period, which is in closer agreement with surface temperatures. However, considering the size and uncertainty of the MSU2R error bars, we advise caution with respect to the significance placed on the absolute trend of +0.07 K per decade. The derivation of trends from multiple satellites is a complex process, particularly considering the fact that MSU2R is an extrapolation from the middle to lower troposphere: subtle, unmodelled effects can significantly alter the trend estimate. The MSU data set needs to be more closely examined, and a more rigorous error analysis should be done.

Although the MSU and radiosondes have provided an extremely valuable air-temperature record for the past few decades, they were originally designed with meteorological objectives in mind, and their ability to measure very small climate variations is limited. There is a need for future climate-monitoring systems that are more accurate and robust. □

Received 24 February; accepted 7 July 1998.

1. Spencer, R. W. & Christy, J. R. Precise monitoring of global temperature trends from satellites. *Science* **247**, 1558–1562 (1990).
2. Spencer, R. W. & Christy, J. R. Precision and radiosonde validation of satellite gridpoint temperature anomalies. Part II: A tropospheric retrieval and trends during 1979–90. *J. Clim.* **5**, 858–866 (1992).
3. Christy, J. R. & McNider, R. T. Satellite greenhouse signal. *Nature* **367**, 325 (1994).
4. Hurrell, J. W. & Trenberth, K. E. Difficulties in obtaining reliable temperature trends: Reconciling the surface and satellite MSU2R trends. *J. Clim.* (in the press).
5. Houghton, J. T. *et al.* (eds) *Climate Change 1995: The Science of Climate Change* (Cambridge Univ. Press, 1996).
6. Jones, P. D. Recent warming in global temperature series. *Geophys. Res. Lett.* **21**, 1149–1152 (1994).
7. Hurrell, J. W. & Trenberth, K. E. Spurious trends in satellite MSU temperatures from merging different satellite records. *Nature* **386**, 164–167 (1997).
8. Hansen, J. *et al.* Satellite and surface temperature data at odds? *Clim. Change* **30**, 103–117 (1995).
9. Christy, J. R., Spencer, R. W. & Braswell, W. D. How accurate are satellite ‘thermometers’? *Nature* **389**, 342–342 (1997).
10. Hansen, J. *et al.* Forcings and chaos in interannual to decadal climate change. *J. Geophys. Res.* **102**, 25679–25720 (1997).
11. Willson, R. C. Total solar irradiance trend during solar cycles 21 and 22. *Science* **277**, 1963–1965 (1997).
12. Wentz, F. J. A well-calibrated ocean algorithm for special sensor microwave/imager. *J. Geophys. Res.* **102**, 8703–8718 (1997).
13. Liebe, H. J. An updated model for millimeter wave propagation in moist air. *Radio Sci.* **20**, 1069–1089 (1985).
14. Gaffen, D. Temporal inhomogeneities in radiosonde temperature records. *J. Geophys. Res.* **99**, 3667–3676 (1994).

Correspondence and requests for materials should be addressed to F.J.W. (e-mail: wentz@remss.com).

## Isotopic evidence for a solar argon component in the Earth’s mantle

R. O. Pepin

School of Physics and Astronomy, University of Minnesota, Minneapolis, Minnesota 55455, USA

Determining the presence of solar argon, krypton and xenon in the Earth’s mantle is important for understanding the source, incorporation mechanism and transport of noble gases in the Earth, as well as the evolutionary history of the Earth’s atmosphere. There are strong indications in the mid-ocean ridge basalt database that solar helium and neon are indeed present<sup>1–3</sup>, and modelling exercises indicate that the compositions of all five noble gases in the Earth’s primordial inventory were solar-like<sup>3–5</sup>. But solar isotopic signatures of the heavier noble gases argon and xenon, which differ significantly from atmospheric compositions,

have appeared only subtly if at all in analyses of mantle-derived samples<sup>6</sup>—their non-radiogenic isotope ratios are generally found to be indistinguishable or only slightly different from those in the atmosphere<sup>7–10</sup>. The first promising isotopic evidence for a solar-like argon component in the Earth’s mantle appeared in a recent analysis of basalt glasses from the Hawaiian Loihi seamount<sup>11</sup>. Here I show that recent measurements<sup>12</sup> of neon and argon isotopes in a suite of mid-ocean ridge basalt samples from the southern East Pacific Rise greatly strengthen the case for the presence of solar argon, and by inference krypton and xenon, in the Earth’s mantle.

Three recent publications bear directly on the issue of a solar component in ocean basalt source reservoirs. Burnard *et al.*<sup>13</sup> used data from a volatile-rich mid-ocean ridge basalt (MORB) glass (‘popping rock’ 2πD43, so named for the audible pops of exploding gas-filled vesicles immediately after it was dredged from the deep Mid-Atlantic Ridge) together with modelling arguments to infer a qualitatively solar-like elemental abundance pattern for all five noble gases in the mantle. They suggested that observation of <sup>38</sup>Ar/<sup>36</sup>Ar ratios between the atmospheric value of 0.1880 and the lower solar ratio would confirm their proposition of the presence of solar Ar, but were pessimistic about the chances for resolving this signature from pervasive atmospheric contamination. Soon thereafter, however, Valbracht *et al.*<sup>11</sup> reported just such a finding in Loihi glasses, with <sup>38</sup>Ar/<sup>36</sup>Ar as low as 0.1848 ± 0.0012 in one stepwise degassing fraction, and further showed that sample-to-sample variations in <sup>38</sup>Ar/<sup>36</sup>Ar and <sup>20</sup>Ne/<sup>22</sup>Ne were correlated in ways highly suggestive of mixing between atmospheric and solar-like endpoint compositions. The third publication, by Niedermann *et al.*<sup>12</sup> on He, Ne and Ar distributions in MORB glasses from the East Pacific Rise (EPR), appeared shortly before the Loihi study. These EPR samples also have low <sup>38</sup>Ar/<sup>36</sup>Ar ratios, here down to 0.1845 ± 0.0018 (1σ) in a total extraction and 0.1814 ± 0.0019 in a thermal release fraction from the same sample (G184D). Niedermann and co-workers noted the presence of these sub-atmospheric values in their data set<sup>12</sup> but did not discuss them further. I have examined the EPR data on a <sup>38</sup>Ar/<sup>36</sup>Ar versus <sup>20</sup>Ne/<sup>22</sup>Ne diagram, and find that they define a remarkably coherent mixing curve between air-derived Ne and Ar and a second component isotopically consistent with current estimates for the solar wind.

The Ne and Ar compositions obtained by Niedermann *et al.*<sup>12</sup> are listed in Table 1 and plotted against each other in Fig. 1. The solar-wind <sup>38</sup>Ar/<sup>36</sup>Ar range of ~0.1786–0.1724 is based on recent analyses<sup>14,15</sup> which indicate substantially lower values for this ratio than an earlier estimate<sup>16</sup>, also shown, of 0.1825. In the following two-component modelling of the Fig. 1 distribution, I take the non-atmospheric component to be solar-wind Ne and Ar within their isotopic uncertainty ranges, and call this ‘solar’ with the assumption that the wind correctly represents the composition of the source supplying these gases to the early Earth. Isotope ratios along an air ↔ solar (a ↔ ☉) mixing trajectory may be shown to be

$$(^{20}\text{Ne}/^{22}\text{Ne})_{\text{calc}} = \left[ \frac{(^{20}\text{Ne}/^{22}\text{Ne})_{\text{a}} + R(^{20}\text{Ne}/^{22}\text{Ne})_{\text{☉}}}{1 + R} \right] \quad (1)$$

$$(^{38}\text{Ar}/^{36}\text{Ar})_{\text{calc}} =$$

$$\left[ \frac{[(^{36}\text{Ar}/^{22}\text{Ne})_{\text{a}} F_{36}^{\text{a}}](^{38}\text{Ar}/^{36}\text{Ar})_{\text{a}} + R[(^{36}\text{Ar}/^{22}\text{Ne})_{\text{☉}} F_{36}^{\text{☉}}](^{38}\text{Ar}/^{36}\text{Ar})_{\text{☉}}}{[(^{36}\text{Ar}/^{22}\text{Ne})_{\text{a}} F_{36}^{\text{a}}] + R[(^{36}\text{Ar}/^{22}\text{Ne})_{\text{☉}} F_{36}^{\text{☉}}]} \right] \quad (2)$$

where  $R = [^{22}\text{Ne}]_{\text{☉}}/[^{22}\text{Ne}]_{\text{a}}$  is the Ne mixing ratio of the two components.  $F_{36}^{\text{a}}$  and  $F_{36}^{\text{☉}}$  are defined and discussed below.

Elemental and isotopic ratios for the two end-point compositions in these equations are listed in Table 1. The factor  $F_{36}^{\text{☉}} = (^{36}\text{Ar}/^{22}\text{Ne})_{\text{mantle}}/(^{36}\text{Ar}/^{22}\text{Ne})_{\text{☉}}$  is included to represent possible elemental fractionation of the solar component before, or accompanying, initial incorporation into its primordial mantle reservoir, or